Journal of Structural Geology 32 (2010) 264–277

Contents lists available at ScienceDirect

Journal of Structural Geology

journal homepage: www.elsevier.com/locate/jsg

Experimental deformation of a single-layer anhydrite in halite matrix under bulk constriction. Part 2: Deformation mechanisms and the role of fluids

G. Zulauf [a,*], J. Zulauf [a], O. Bornemann [b], F.E. Brenker [a], H.E. Höfer [a], M. Peinl [a], A.B. Woodland [a]

[a] Institut für Geowissenschaften, Universität Frankfurt a.M., Altenhöferallee 1, D-60438 Frankfurt a.M., Germany
[b] Bundesanstalt für Geowissenschaften und Rohstoffe, Stilleweg 2, D-30655 Hannover, Germany

ARTICLE INFO

Article history:
Received 23 March 2009
Received in revised form
23 November 2009
Accepted 2 December 2009
Available online 23 December 2009

Keywords:
Experimental deformation
Asse halite
Gorleben anhydrite
Rock salt
Fluids

ABSTRACT

Composite natural samples, consisting of a single layer of anhydrite, embedded in matrix of rock salt, were experimentally deformed at temperature, $T = 345$ °C and strain rate, $\dot{e} = 10^{-7}$ s^{-1}. The geometry and kinematics of folds and boudins, which affect the stiff anhydrite layers, were described in Part 1 of the present study (Zulauf et al., 2009). The microfabrics, deformation mechanisms, and the role of fluids are treated in the present paper. Anhydrite was deformed under brittle–viscous conditions as is indicated by fracturing, twinning, and local recrystallization, the latter based on strain-induced grain-boundary migration. Viscous deformation of halite was accommodated by slip on {110}⟨110⟩ which led to formation and rotation of subgrains and a striking 001-maximum parallel to the long axis, *X*, of the strain ellipsoid. Differential stress obtained from subgrain size of halite is largely consistent with stresses recorded by the load cells of the machine (<5 MPa).

Despite of the high deformation temperature and the low water content of the starting samples, NaCl brine and hydrocarbons, expelled from fluid inclusions of both halite and anhydrite, led to hydraulic fracturing and redistribution of matter. The fluids migrated along newly formed microfractures in anhydrite and along halite–anhydrite boundaries. Released hydrocarbons and NaCl brine were redeposited in open space of neck domains in the form of black organic coatings (condensate) and fine-grained halite, respectively. As these fluid-controlled phenomena are common in salt domes of northern Germany, and released fluids may led to contamination of bed rock and biosphere, the results of the present study should be important for workers who are dealing with radioactive waste deposits in rock salt.

1. Introduction

Rock salt in undisturbed state is characterized by low porosity (<<0.5%), low permeability (<<10^{-20} m^2) and low water content (<0.1 vol%) (Popp et al., 2007). For these reasons rock salt is commonly used as host rock for storage of gas and crude oil, and is also considered for the disposal of radioactive waste. However, deforming rock salt may change its properties considerably. Transient and steady-state flow properties of rock salt are thus important for analyses of salt tectonics and geotechnical engineering problems. The deformation mechanisms of naturally deformed rock salt have recently been reviewed by Urai and Spiers (2007). There is evidence that low temperature dislocation glide and dislocation creep are common deformation processes. Of particular importance are fluids which support solution–precipitation creep and induce dynamic recrystallization by fluid-assisted grain-boundary migration (e.g. Urai et al., 1987; Spiers et al., 1990; Spiers and Schutjens, 1990; Hickman and Evans, 1991; Spiers and Carter, 1998; Watanabe and Peach, 2002; Schenk and Urai, 2004; Ter Heege et al., 2005b; Schléder and Urai, 2007).

Rock salt is seldom free from mechanical anisotropy. There are layers of anhydrite or layers of dry shale which are significantly stronger than halite resulting in inhomogeneous strain. The laminated salt rocks can exhibit considerable different mechanical properties compared to pure rock salt (Li et al., 2007). The interfaces between the intercalated competent layers and rock salt are particularly important because they are sites were stress, strain and deformation mechanisms change. Moreover, the contacts between rock salt and stiff layers, such as anhydrite, could act as pathways for migrating fluids which are important for the deposition of radioactive waste in salt stocks (e.g. Bornemann et al., 2008).

The present paper presents microfabrics of experimentally deformed samples consisting of a single stiff layer of Gorleben anhydrite embedded in weaker matrix of Asse halite. The macroscopic geometry of boudins and folds has already been published in

* Corresponding author.
E-mail address: g.zulauf@em.uni-frankfurt.de (G. Zulauf).

0191-8141/$ – see front matter © 2009 Elsevier Ltd. All rights reserved.
doi:10.1016/j.jsg.2009.12.001

Part 1 of the present study (Zulauf et al., 2009). The anhydrite layer, oriented parallel to the major stretching axis, *X*, was macroscopically deformed by fracturing, whereas halite behaved viscously. At an advanced state of constriction ($e_x > 90\%$) a strong increase in strain hardening of halite led to a transient tension fracture that healed up and was shortened by folding during the final phase of viscous deformation. Tiny prismatic anhydrite inclusions disseminated inside the halite matrix were reoriented during constriction resulting in a linear grain-shape fabric (Fig. 1). 3D-images of the anhydrite layer, based on computer tomography, revealed rare kink folds with axes subparallel to *X*, and boudins which result from tension fracture. With increasing layer thickness, H_i, the width of boudins, W_a, increases linearly and the normalized width of boudins ($W_d = W_a/H_i$) is almost constant at 1.5 ± 1.0 (Zulauf et al., 2009).

The microfabrics observed in the deformed samples will be used to deduce the deformation mechanisms that operated in halite and anhydrite during the experimental runs. It will be shown that fluids have played a significant role during deformation. The microfabrics further explain why the contacts between competent anhydrite and weaker halite play a key role for fluid transport in salt domes.

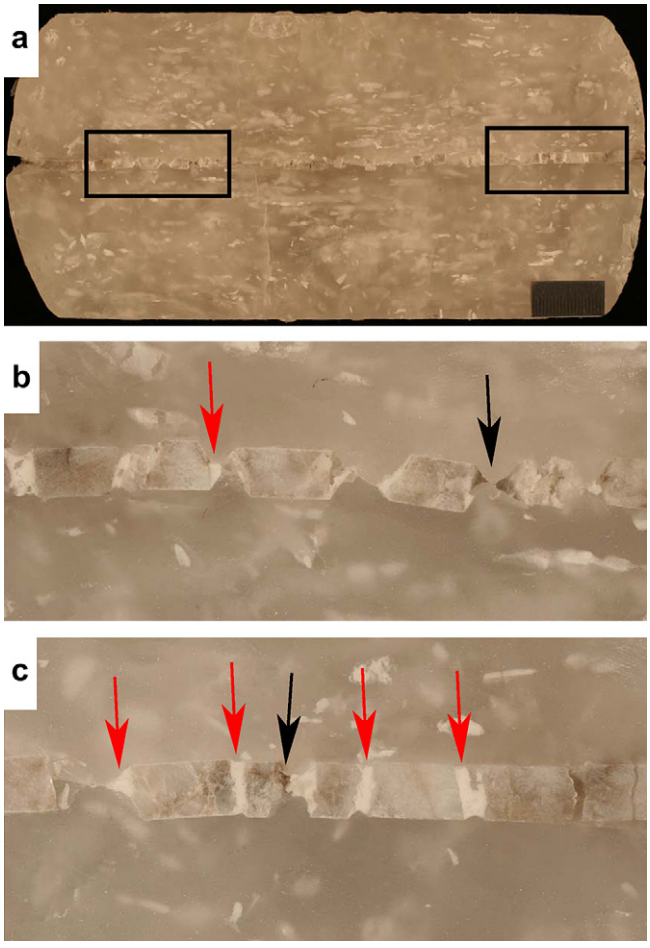

Fig. 1. (a) Section of deformed sample cut parallel to the *X*-axis and perpendicular to anhydrite layer. Initial thickness, H_i, of anhydrite layer = 1.5 mm. Note boudinage of anhydrite layer and strong shape-preferred orientation of small anhydrite inclusions in halite matrix. Black bar = 1 cm. (b) and (c) Close-up views of areas marked by black frame in (a). Necks between the anhydrite boudins which are not entirely filled with viscous halite are different. Some are mineralized by fine-grained halite which should have precipitated from fluid phase (red arrows). Others are still open and coated by dark organic matter (black arrows). (For interpretation of the references to colour in this figure legend, the reader is referred to the web version of this article.)

As the deformation mechanisms in rock salt are similar to those of silicate rocks deformed at high temperature and pressure, rock salt can be used as analogue material for silicates (e.g. Guillopé and Poirier, 1979; Hiraga and Shimamoto, 1987).

2. Methods

2.1. Experimental setup

We deformed composite samples consisting of natural halite as matrix and natural anhydrite as an embedded layer. All samples were delivered by BGR Hannover. For details on sample preparation, see Zulauf et al. (2009). Halite samples of the Asse borehole of northern Germany (800 m level, Speisesalz Na2SP) have been used for the experiments. The internal structure of the Asse salt dome has been described by Essaid and Klarr (1982). The anhydrite samples used for our experiments were collected from the Gorleben deep borehole 1004 (Bornemann et al., 2008).

Pure constrictional deformation of the composite halite–anhydrite samples was performed using a new thermomechanical deformation rig that is described in detail in Zulauf et al. (2009). The anhydrite layer was oriented parallel to the *X*-axis of the finite strain ellipsoid. Deformation conditions during each run were as follows: $T = 345\ ^\circ C$, $\dot{e} = 2–4 \times 10^{-7}\ s^{-1}$, $e_{Y=Z} = -33\%$ and $e_x = 122\%$. The initial thickness of the anhydrite layer, H_i, varies from 0.8 to 2.5 mm. Only in that run where the initial thickness of the anhydrite layer was set at 2.5 mm, the deformation of the sample was limited to a finite strain $e_{Y=Z} = -17\%$ and $e_x = 44\%$, respectively, because the pre-scribed stress limit of the machine was reached (see below).

2.2. Microfabric studies

Thin and thick sections were prepared from undeformed halite and anhydrite samples and from sections of deformed samples which are oriented parallel and perpendicular to the *X*-axis of the finite strain ellipsoid, respectively. To reveal the grain and subgrain boundaries in halite, we used the method described by Urai et al. (1987). After polishing the sections with colloidal diamond dispersed in oil (0.25 and 1 μm), the sections were lightly etched for 30 s using a 95% saturated NaCl solution containing 0.8 wt% $FeCl_3 \times 6H_2O$. Subsequently the etchant was removed from the surface using a powerful jet of *n*-hexane, and the section was dried in a stream of warm air.

Less deformed natural slabs and experimentally deformed slabs of samples with initial layer thickness H_i of 1.5 and 2.0 mm, respectively, were treated by gamma-irradiation in the Research Reactor of Forschungszentrum Jülich, using a technique similar to that described by Schléder and Urai (2005). Irradiation was carried out for 155 days at a temperature of 100 °C and with an average dose rate of 0.5 kGy/h to a total dose rate of 2 MGy. The initially clear halite developed various shades of blue. The colour intensity in the halite crystals is heterogeneous because of heterogeneous distribution of solid solution impurities and other crystal defects (Urai et al., 1987; Schléder and Urai, 2005, and references therein).

The thin sections were studied using reflected and transmitted light microscopy. Subgrains in halite have been found in etched samples using transmitted or reflected light. To determine the average diameter of subgrains, *D*, from transmitted light photographs of irradiated thin sections and from reflected and transmitted light photographs of etched thin sections, the outlines of the subgrains were digitized, and subsequently the area of the grains was determined using image analysis software DiAna. From the grain area the average grain diameter was obtained by calculating the diameter of a circle equivalent in area to that of the subgrain.

To reveal organic matter inside fluid inclusions, fractures and in open pore space of boudin necks, the sections were further investigated using fluorescence microscopy under reflected light. The fluorescence studies allow the distinction of liptinitic (fluorescent) from humic amorphous (nonfluorescent) organic matter (Tissot and Welte, 1984).

Due to the limited depth of field of brightfield microscopes, it is seldom possible to image large 3-D objects, such as cavities in neck domains or diving grain boundaries, entirely in focus. By optically sectioning the specimen, however, the in-focus information at the specimen's surface can be acquired over a range of images, which can then be processed to generate a single in-focus image. The idea is to merge a stack of micrographs (6–18 in the present study) taken at different focal positions (aligned along the optical axis) into a single, entirely focused composite image. In the present case we used the software *ImageJ* and the *Complex wavelet-based method* developed by Forster et al. (2004) to produce in-focus composite images.

2.3. Electron backscatter diffraction (EBSD) analyses

The application of electron backscatter diffraction to the study of halite microfabrics provides information about a lattice preferred orientation in rock salt (e.g. Pennock et al., 2005; Bestmann et al., 2005; Schléder and Urai, 2007). This technique was applied to polished sections cut parallel to the *X*-direction using an in-house equipment. The samples were coated with carbon up to a thickness of about 4 nm to reduce charging effects. Crystallographic orientation data were obtained from EBSD patterns using a JEOL JSM-6490, typically operating with an acceleration voltage of 15 keV and beam current of 8 nA. The EBSD patterns were indexed with the CHANNEL 5 software (HKL Technologies) using the file for halite consisting of 46 lattice planes. Multiple beam maps were used to map the specimen. For an individual map, data points were collected on a rectangular area at a fixed step size of 13 μm by moving the sample and keeping the beam stationary. After the mapping, the individual maps were stitched together using the CHANNEL 5 software. The texture is displayed in form of inverse pole figures which are plotted as contour maps over the standard triangle for the cubic symmetry. A contour of unity corresponds to a randomly orientated sample.

2.4. Raman spectroscopy

Raman spectra were recorded from fluid inclusions and neck domains using a Renishaw RM-1000 micro-Raman spectrometer operating in backscatter geometry. The spectrometer is equipped with two lasers having 532 nm and 633 nm wavelengths, respectively. The laser was focused through a 50× objective, giving a spot size of ~2–5 μm. The Raman shift is measured as the wave number difference between incident and scattered light. The wave number is defined as the reciprocal wavelength and is given in cm^{-1}. The spectrometer was calibrated using the 520 cm^{-1} line of silicon. Spectra were obtained with variable counting times either in static or scanning mode, depending on the desired wave number range.

3. Results

3.1. Microfabrics

3.1.1. Anhydrite of initial samples

There are two different types of anhydrite in the deformed samples: the primary inclusions of anhydrite inside Asse halite, and the Gorleben anhydrite that was sandwiched between the matrix of Asse halite forming the competent layer.

Inclusions of anhydrite with grain size up to 4 mm are present within the halite grains and along halite grain boundaries. These anhydrite inclusions do not show a shape-preferred orientation and are largely free from deformation fabrics. Some of the inclusions show twinning on the {101} planes.

The grain size of anhydrite of the initial Gorleben samples varies considerably from <100 μm–10 mm. Most of these grains show primary growth fabrics and a dirty habitus, the latter resulting from numerous fluid inclusions and opaque phases (Figs. 2a,b and 3a). The shape of the dark inclusions is sometimes rectangular or even quadratic suggesting pseudomorphic growth after halite. Most of the inclusions show fluorescence (Fig. 3b). A few of the fluid inclusions revealed a bright margin resulting from fluorescence whereas the core is dark. Rosette shaped aggregates of anhydrite are frequently present on almost all scales (Fig. 2a). The anhydrite rosettes are partly truncated by highly lobate seams which are rich in fluid inclusions and opaque phases. These seams are common in Zechstein anhydrite and reflect localized dissolution–reprecipitation creep (Bäuerle, 1998; Bornemann et al., 2008). Local, but weak crystal plastic strain is documented by rare twinning on the {101} planes and by weak bending of long-prismatic crystals. There are few anhydrite grains which are almost clean and free from deformation fabrics. These crystals grew late within small veins or in open pore space.

3.1.2. Experimentally deformed anhydrite

The primary anhydrite inclusions inside Asse halite matrix were reoriented due to constriction with the long axis being aligned subparallel to the *X*-axis (Fig. 1a). As these inclusions were flowing in much weaker halite, they do not show noticeable internal crystal plastic strain. However, there is strong evidence for fluid-controlled reactions at the anhydrite/halite interface and for fracture boudinage that will be described below.

The principal deformation fabric of experimentally deformed layers of Gorleben anhydrite is fracturing along the cleavage planes. Cataclastic deformation of anhydrite in the neck domains results in strong grain size reduction with porphyroclasts being embedded in the viscous halite matrix (Fig. 2c). The size of the porphyroclasts is as low as 20 μm. Most of the boudins contain microfractures (Fig. 2f, 3c), some of which are filled with organic matter as is shown by the bright color when using fluorescence microscopy (Fig. 3d).

Crystal plastic strain is recorded by undulatory extinction, deformation twins, bending of long-prismatic crystals, and serrated grain boundaries (Fig. 2d). Serrated grain boundaries reflect strain-induced grain-boundary migration which results in smaller recrystallized grains. In contrast to the host grains these new grains are largely free from impurities (Fig. 2e). Most of the recrystallized grains are almost isometric with diameters ranging from 20 to 70 μm. Some of them display undulatory extinction. The twin density varies considerably. Grains which show extremely high density of twins (up to 800 per mm) are restricted to high-strain domains of the neck areas. Such twins are oriented perpendicular to the long axis of the anhydrite crystals and thus differ considerably from those of naturally deformed anhydrite where twins are oriented parallel to the long side (along {101} planes). At the interfaces to the halite matrix, twins and cleavage planes are frequently bent due to the drag of the flowing halite (Fig. 2f).

3.1.3. Halite matrix of initial samples

For the present studies we selected samples of Asse halite which are largely free from a grain-shape fabric. The size of the halite grains is 4.2 ± 2 mm. The grains are almost free from crystal plastic strain as is revealed by etched and irradiated samples. Grain boundaries are either straight or weakly lobate (Fig. 4a). Subgrains are rare and largely restricted to the surroundings of rigid anhydrite inclusions. The size of these subgrains is similar to those produced by the

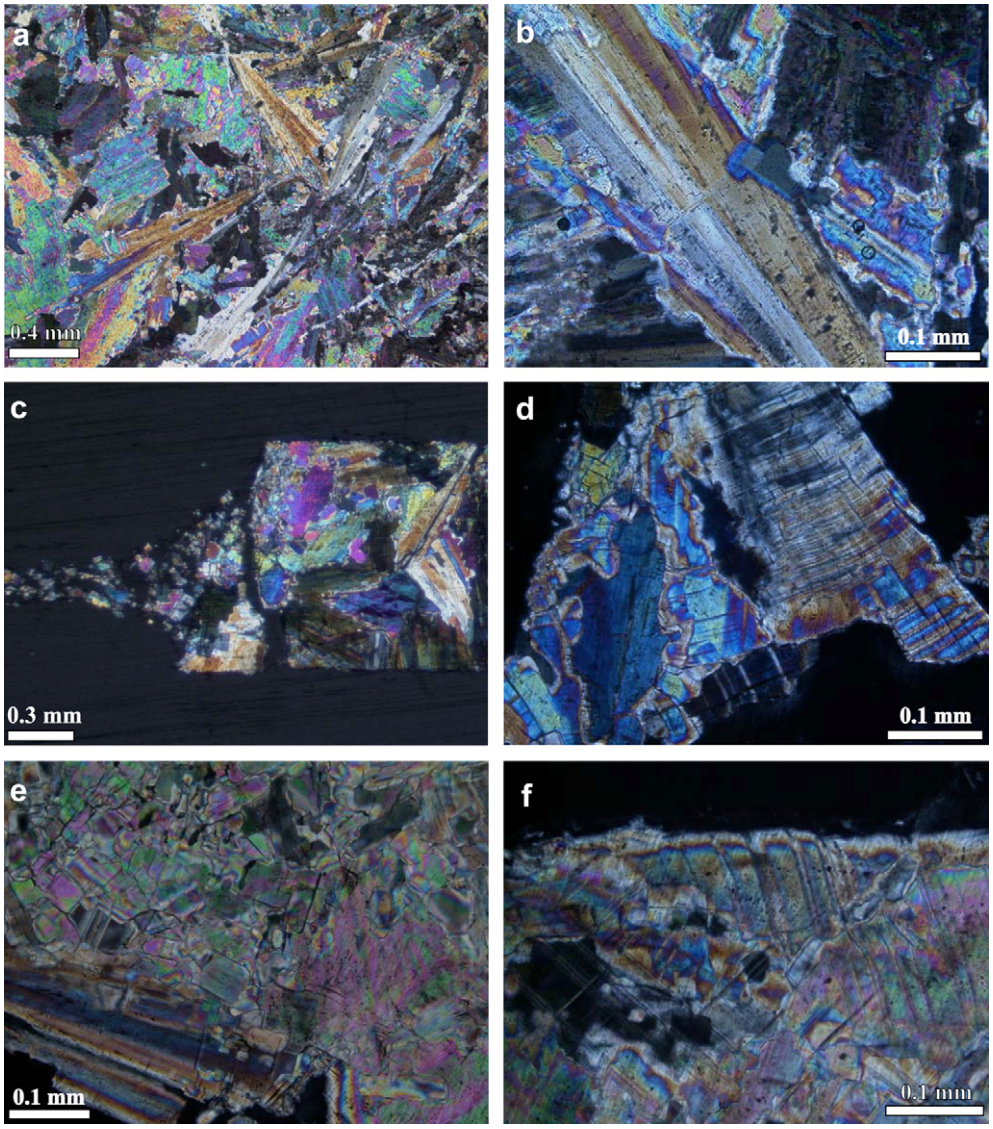

Fig. 2. Photomicrographs showing microfabric of initial and experimentally deformed Gorleben anhydrite. All micrographs were produced from sample K1.1 using transmitted light and crossed polarizers. (a) Typical static growth fabric of initial anhydrite. Long-prismatic crystals are almost undeformed. Note the large number of fluid inclusions and other impurities inside the grains. (b) Close-up view of (a) showing undeformed large crystals of anhydrite which include numerous fluid inclusions and opaque phases. (c) Cataclastic deformation and strong grain-size reduction of anhydrite in neck domain. Anhydrite boudin and anhydrite porphyroclasts in neck domain are surrounded by viscously deformed halite that is dark in the photomicrograph. Section cut parallel to the *X*-axis and perpendicular to the layer. (d) Microstructures of experimentally deformed anhydrite indicate fracturing, twinning and strain-induced grain-boundary migration inside the boudin. Crystal plastic strain is also indicated by undulatory extinction of large crystals. Note the high density of twins affecting the large crystal in the right part of the photograph. Section cut parallel to the *X*-axis and perpendicular to the layer. (e) Large old anhydrite crystals (lower part) show fractures and impurities and are replaced by fine-grained new grains which are almost isometric and free from impurities (upper part). Section cut parallel to the *X*-axis and perpendicular to the layer. (f) Drag of anhydrite twins along boundary to halite matrix (upper part of photograph). The internal part of anhydrite is affected by shear fractures, bending and undulatory extinction. Section cut parallel to the *X*-axis and perpendicular to the layer. (For interpretation of the references to colour in this figure legend, the reader is referred to the web version of this article).

experiments (see below). Analyses of the subgrain size of three different domains of initial sample K2.2 yielded the following values, where N is the number of grains considered: 60 ± 12 μm ($N = 33$), 73 ± 21 μm ($N = 36$), 80 ± 27 μm ($N = 56$). Carter et al. (1982), on the other hand, found subgrain sizes in Asse halite of ca. 220 μm.

A striking feature of all of the initial halite samples is the presence of grain-boundary fluid inclusions which have already been described in detail from other Asse samples (Urai et al., 1987). Compared to the experimentally deformed samples, these fluid inclusions are regularly distributed along the grain boundaries in most of the initial samples. Based on their shape, three types of fluid inclusions can be distinguished (Fig. 4c). There are large and small inclusions which occur as bubbles (0-D inclusions). These bubbles are frequently coalesced resulting in a network of straight or slightly bent tubes (1-D inclusions). In some cases the fluid tubes may fuse into a dark film-like sheet (2-D inclusions). Fig. 4c shows such a fluid film which is displaced along a sinistral shear plane. Note that the shear plane is also replete with small 0-D inclusions. Fig. 4d shows the spatial distribution of the fluid-decorated grain boundaries with the different grey values reflecting the different levels of topographic height within the investigated section. Note that the topography shows the same sinistral displacement like as the black fluid film.

Investigations using fluorescence microscopy revealed that most of the fluid inclusions consist of at least two different phases (Fig. 4e,f). One of these phases is dark, the other appears bright. In most cases the dark matter forms the central part of the inclusion which is surrounded by the bright matter resembling fried eggs.

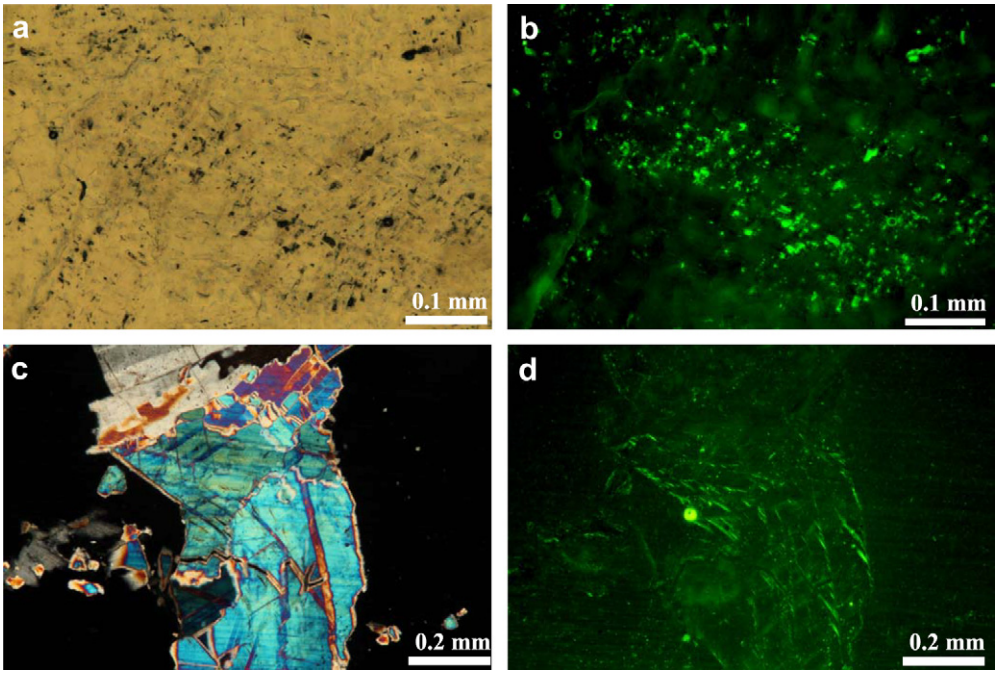

Fig. 3. (a) Fluid inclusions inside large crystals of intact Gorleben anhydrite of starting sample; transmitted light, parallel polarizers. (b) Same view as in (a) but using fluorescence microscopy. Note that almost all inclusions show fluorescence. Reflected light. In-focus composite image based on stack of 10 photomicrographs. (c) Anhydrite boudin showing microfractures, twins and kink bands. Transmitted light, crossed polarizers. (d) Same view as in (c) but using fluorescence microscopy. Note that microcracks are filled with organic matter as is shown by fluorescence. Reflected light. In-focus composite image based on stack of 13 photomicrographs. (For interpretation of the references to colour in this figure legend, the reader is referred to the web version of this article).

Note that the bright spot inside the dark matter does not mark a third phase but is an apparent effect due to internal optical reflection/refraction. It is obvious from the fluorescence images that the bright matter in the outer parts of the inclusions may fuse into tubes or films which still include spots of the dark matter, the latter forming 0-D inclusions inside the films. As the outer parts of the inclusions show fluorescence, they should consist of organic matter. Organic matter is also confirmed by the Raman spectrum which shows the presence of methane (Fig. 5a). The central dark part of the inclusions is probably NaCl bearing brine as is revealed by the halite peak in the Raman spectrum.

3.1.4. Experimentally deformed halite matrix

All of the deformed samples show a strong prolate grain-shape fabric of both halite and anhydrite inclusions (Fig. 1a). In sections cut perpendicular to the *X*-axis, the grain boundaries of halite are no longer straight but strongly lobate due to constrictional folding. In irradiated sections, these folded grain boundaries occur as light brownish lines, up to 0.1 mm in width, with the fluid inclusions in the centre (Fig. 6a,b). In irradiated samples cut parallel to the *X*-axis the grain boundaries of halite are largely straight (Fig. 6c). In contrast to the initial samples, however, the halite grains are strongly elongated due to crystal plastic deformation. In irradiated samples cut parallel to the *X*-axis crystal plastic strain is frequently recorded by two sets of bright lines which are orthogonal to each other resulting in a rectangular grid with the *X*-axis forming the angle bisector (Fig. 6c). The spacing of these bright lines ranges from 50 to 100 μm. At a closer view the bright lines are subgrain boundaries which are forming a chessboard pattern (Fig. 6d). This is the common microstructure inside the halite grains in sections cut parallel to the *X*-axis. Subgrains with more irregular boundaries are also present (Fig. 6e), particularly in sections cut perpendicular to the *X*-axis. The subgrain size varies between 45 ± 14 μm and 69 ± 22 μm (Table 1). The subgrain size decreases significantly adjacent to rigid anhydrite inclusions. EBSD analyses of the halite matrix in sections cut parallel to the *X*-axis and perpendicular to the layer revealed a striking 001-maximum parallel to the *X*-axis as is shown in inverse pole figure (Fig. 7). As constriction is axisymmetric, the inverse pole figures describe the texture completely.

The fluid inclusions along grain boundaries are stretched and less regularly distributed than those of the initial sample (Fig. 6f). Deformation of fluid inclusions is particularly strong in high-strain domains such as the boundaries to rigid anhydrite where fluid inclusions are enriched in the form of film-like dark sheets. Thus, the competent anhydrite may form reservoir traps for fluids derived from halite. These fluid inclusions show still fluorescence under UV light. Finally it has to be emphasized that the transient tension gashes in halite, which have formed subperpendicular to the *X*-axis at $e_x > 90\%$ (Zulauf et al., 2009), are partly filled with opaque organic matter (Fig. 8a) which fluoresce weakly.

3.1.5. Neck domains and halite/anhydrite interfaces

Boudinage of anhydrite did not only affect the layer of Gorleben anhydrite that was sandwiched between Asse halite, but small elongate inclusions of primary anhydrite inside the Asse halite matrix also boudinaged (Fig. 8f). The necks between these small boudins are in most cases entirely filled with halite. In a few cases, however, the necks show open spaces with walls coated by black matter (Fig. 8c). The necks between the boudins of the sandwiched layer of Gorleben anhydrite show similar features. Some of them are entirely filled with halite, which was flowing viscously into the necks sometimes including streaks of fractured anhydrite (Fig. 2c). Some necks are still open or are only partially filled with viscous halite. Also in these cases the walls of the open space are coated with black matter (Figs. 1b,c and 8b). As this black coating fluoresces, it should consist of organic matter. This assumption is supported by Raman spectroscopy which indicates the presence of methane (Fig. 5b). Open space in neck domains is in some cases also filled with fine-grained white material (Fig. 1b,c), the grain size being less than ca. 5 μm. XRD analyses have shown that this white

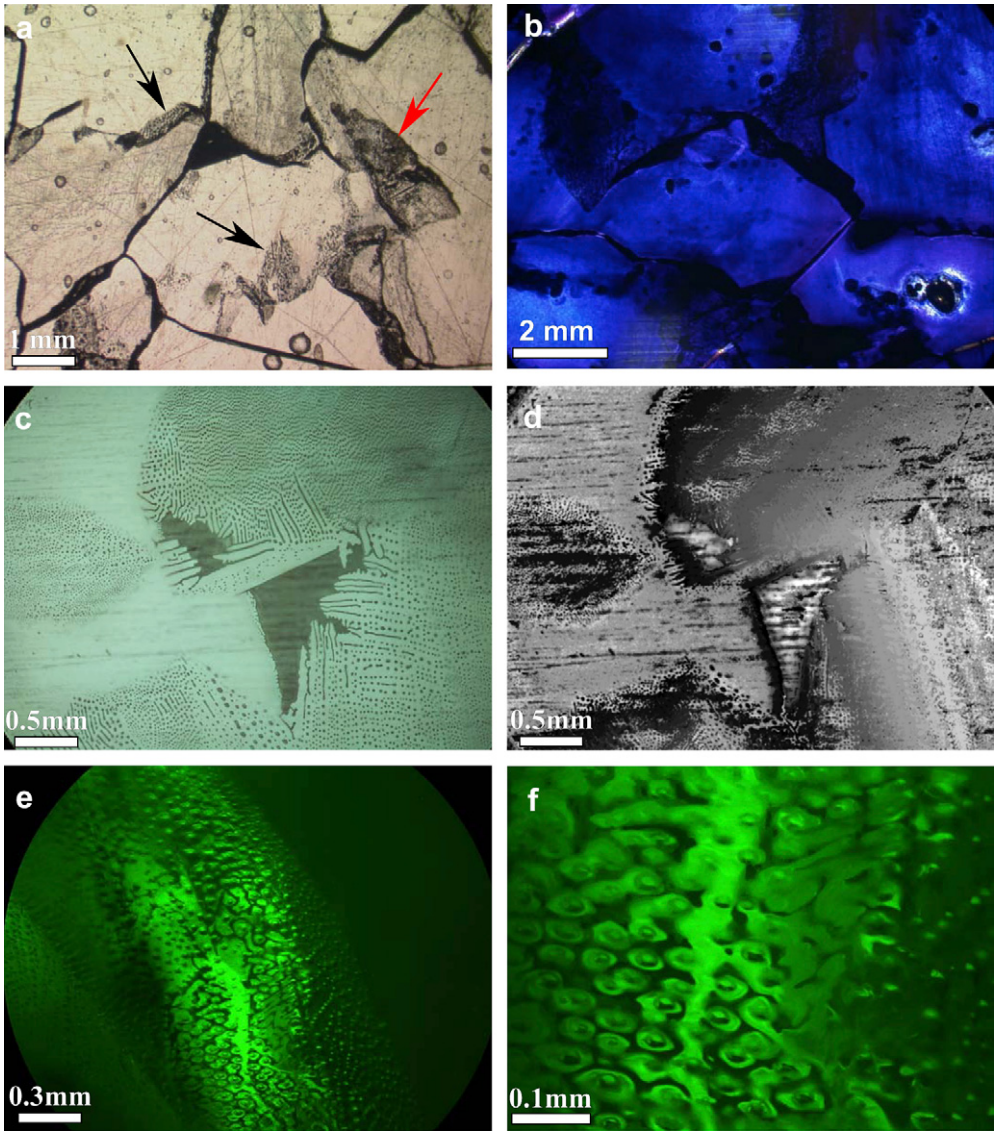

Fig. 4. Photomicrographs of starting samples of Asse halite (Na2SP Speisesalz) used for experiments. (a) Halite showing slightly lobate grain boundaries which are sites of fluid inclusions. Dirty domains inside halite grains are less inclined grain boundaries which are rich in fluid inclusions (see black arrows). Small inclusion of anhydrite is indicated by red arrow. Parallel polarizers and transmitted light. (b) Irradiated sample showing no significant intracrystalline deformation. (c) Grain-boundary decorated with fluid inclusions. The fluid inclusions are present as single bubbles, channels, and film. Note the sinistral displacement of the fluid film with the shear zone showing much smaller fluid inclusions. In-focus composite image based on stack of 16 photomicrographs. Parallel polarizers and reflected light. (d) Same image like (c) showing calculated topography of the fluid-decorated grain boundaries by different shades of grey. Dark is higher, bright is lower. (e) Fluorescence image of grain-boundary fluid inclusions of halite. Reflected light. In-focus composite image based on stack of 10 photomicrographs. (f) Close-up view of (e) showing outer bright rim of fluid inclusions, consisting of organic matter, and dark core consisting of NaCl brine. Bright spot inside dark core is a reflex. In-focus composite image based on stack of 8 photomicrographs. (For interpretation of the references to colour in this figure legend, the reader is referred to the web version of this article.)

material consists of halite. In thin sections it is further obvious that few opaque phases and numerous tiny fluid inclusions are irregularly distributed inside this fine-grained neck infill, and some of the walls of these halite-filled necks are also coated with black organic matter (Fig. 8e). In sections cut parallel to the *X*-axis and perpendicular to the anhydrite layer, the shape of the open spaces between boudins is strikingly different. In cases where the width of the neck is large, the open spaces are double triangles that taper from the boudin walls towards the centre of the neck (Fig. 8b). The open spaces in narrow necks are almost rectangular.

Another interesting feature is that the halite matrix adjacent to anhydrite boudins is comparatively enriched in fluid inclusions. This holds for both types of anhydrite boudins, large boudins, resulting from boudinage of the layer of Gorleben anhydrite, and small boudins consisting of primary anhydrite that was reoriented during constriction with the long axis subparallel to the *X*-axis (Fig. 8f). Rosette-shaped fluid-inclusion trails which grew almost radial into the halite matrix from a fluid source located inside the anhydrite boudin (Fig. 8d) suggests that fluids were expelled from Gorleben anhydrite into the adjacent halite matrix. The same holds for the primary anhydrite inclusions. Most of these inclusions show a striking corona of fluid inclusions (Fig. 8f). In some cases there is evidence that fluids have migrated into halite along radial cracks, the latter being filled with anhydrite or with dark matter (Fig. 8c).

3.2. Piezometry using subgrain size of halite

Experimental deformation of various minerals and rocks revealed a strong correlation between the steady-state subgrain size, D, and flow stress, σ, (e.g. Twiss, 1977). Based on calibrations

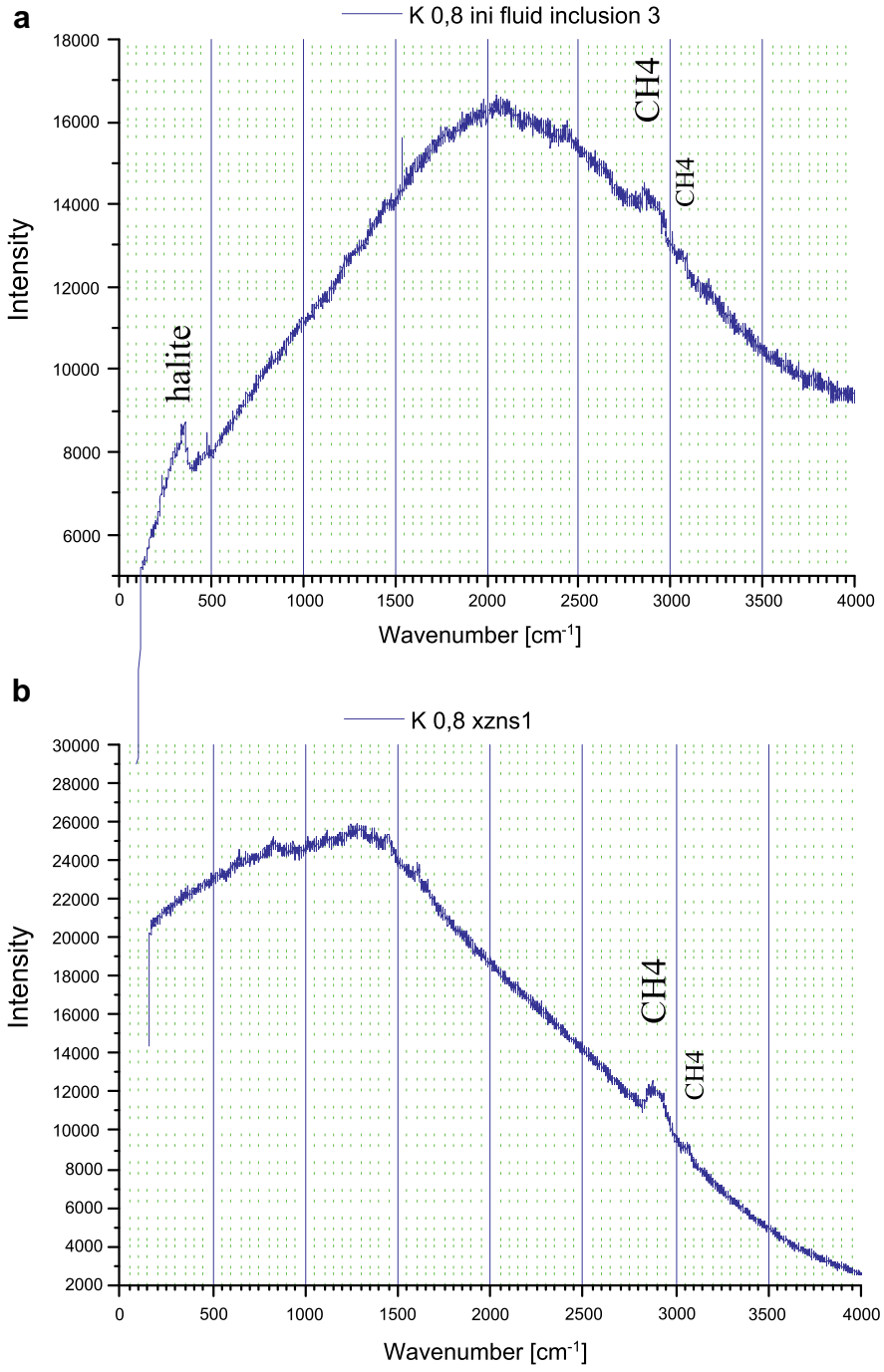

Fig. 5. Results of Raman spectroscopy. (a) Grain-boundary fluid inclusion of initial Asse halite showing peaks characteristic for halite (250 and 350 cm^{-1}) and for methane (2909, 3016 and 3062 cm^{-1}). (b) Dark organic coating of open space of neck domain showing peaks characteristic for methane similar to those depicted in (a).

obtained by Carter et al. (1993) and Franssen (1993) using experimentally deformed rock salt, this relationship can be written as

$$D[\mu m] = 215\sigma'^{-1.15}[Mpa] \quad (1)$$

(Schléder and Urai, 2005). Eq. (1) has been used for estimating the stress, σ', in deformed Asse halite that was compared with the actual stress values, σ, recorded by both single-point load cells during each experimental run. The number of grains considered in one sample ranges from 80 to 300. The following conditions should be met when using this method of piezometry: (i) the size of subgrains should not be influenced by secondary phases like anhydrite; (ii) the subgrains must reflect a steady-state deformation fabric and should not be influenced by postkinematic annealing (Twiss and Moores, 1992, p. 412).

The first prerequisite is large fulfilled. The second prerequisite, however, is only partly fulfilled because of strain hardening, particularly at advanced state of strain. A second problem is the influence of the stiff anhydrite layer.

The subgrain size of experimentally deformed Asse halite varies from 45 ± 14 μm to 69 ± 22 μm (Table 1). The stress obtained from the subgrain size using Eq. (1) is also listed in Table 1 and is further shown in the stress-strain plots (shaded arrays) besides the curves which display the stresses recorded by the load cells during the

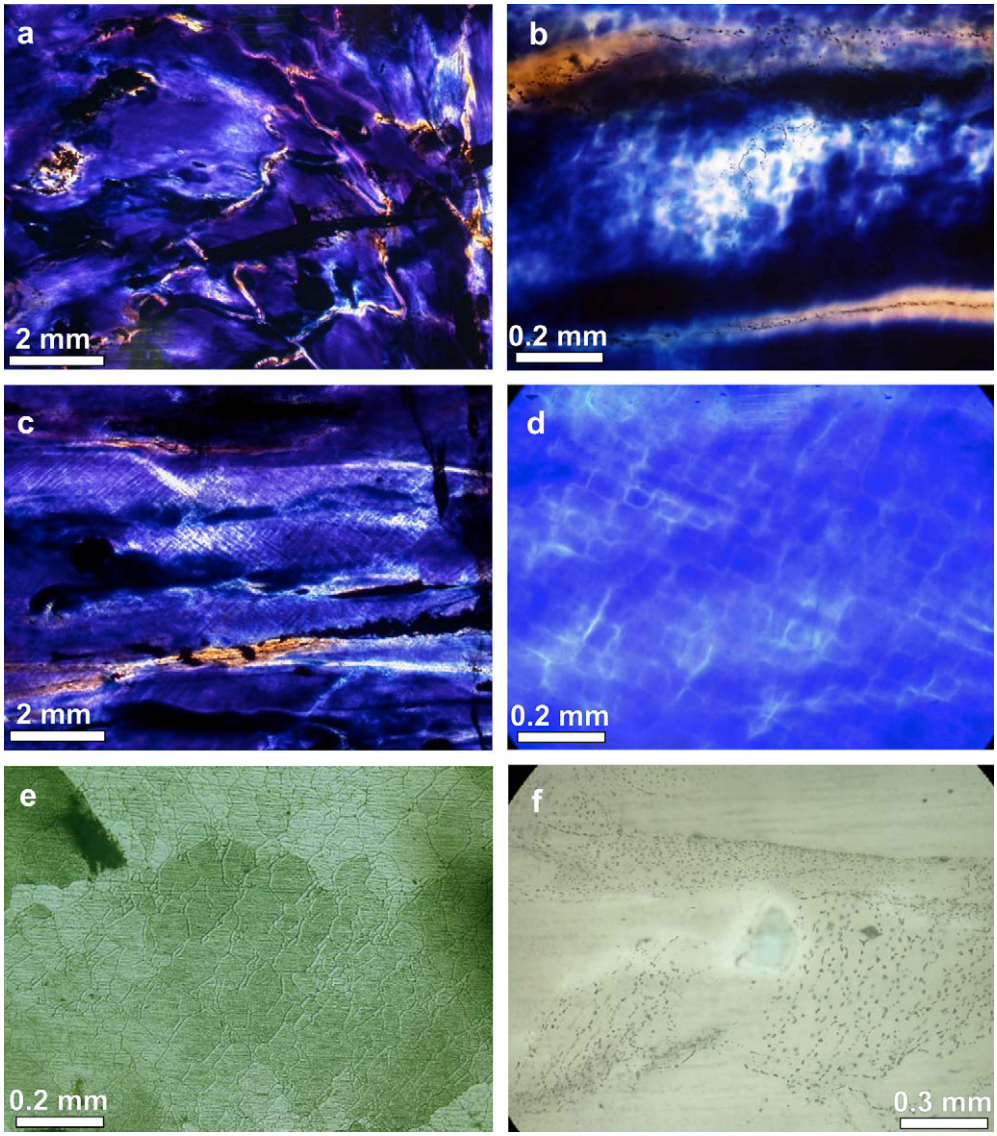

Fig. 6. Photomicrographs of experimentally deformed Asse halite using transmitted light and parallel polarizers. All samples are irradiated apart from sample shown in (e and f). (a) Strongly lobate grain boundaries (white to brownish lines) result from constrictional folding. Section cut perpendicular to the *X*-axis. Dark patches are inclusions of anhydrite. Sample K2.2. (b) Close-up view of (a) showing fluid inclusions along two sheared grain boundaries of halite which are subhorizontal in the picture. The space in between these grain boundaries is characterized by less distinct subgrains. Note the polygonal outline of fluid-inclusion trails which might indicate subgrain or even grain boundaries. (c) Two sets of closely spaced bright lines, which are orthogonal to each other, are forming a rectangular grid. These lines are interpreted as slip planes. Section cut parallel to the *X*-axis and perpendicular to the anhydrite layer. Sample K2.2. (d) Close-up view of (c) showing subgrain boundaries of halite (white lines) which are orthogonal to each other resulting in a chessboard pattern. (e) Less regular subgrains (white lines) in section cut parallel to the *X*-axis and perpendicular to the anhydrite layer. Note the grain boundaries decorated with fluid inclusions. Sample K1.5. (f) Deformed trails of grain-boundary fluid inclusions of Asse halite. Note the irregular distribution and the stretch of most of the inclusions as compared to initial samples. (For interpretation of the references to colour in this figure legend, the reader is referred to the web version of this article).

individual runs (Fig. 9). The maximum and minimum stress obtained by the subgrain sizes of the individual samples is 5.97 MPa (sample K2.5, Fig. 9f) and 2.11 MPa (sample K2.2, Fig. 9e), respectively. In those cases where the curves of the actual stresses show a large deviation (Fig. 9a,d,f), the stress range obtained from subgrains is more consistent with the red curves which reflect the higher stresses measured in the direction parallel to the anhydrite layer (with the load cell being placed on the layer). Particularly in samples K1.85 (Fig. 9d) and K2.5 (Fig. 9f) the average stresses obtained from subgrain size (3.46 MPa and 3.66 MPa, respectively) are close to the less inclined slopes of the red curves which reflect almost steady-state deformation. In the other cases, where both stress curves (red and black) are close to each other throughout the entire runs, the stress ranges calculated using the subgrain sizes differ from the stresses measured using the load cells. In sample K1.1 (Fig. 9b) the stresses obtained by the subgrains are in the range where significant strain hardening was active after a strain of ca. 25% had been achieved. In sample K1.5 (Fig. 9c) the average stress obtained by the subgrain size (2.80 MPa) is in the range before significant strain hardening was initiated. In sample K2.2 the stresses recorded by the subgrains reflect the less inclined slope of the actual stresses (Fig. 9e). Thus, the stress values calculated by the subgrain size of Asse halite can be used at least as an order of magnitude estimate.

4. Discussion

4.1. Deformation mechanisms in anhydrite

The microfabrics observed in anhydrite result from deformation mechanisms that were active in nature and during the

Table 1
Deformation parameters of thermomechanical runs and piezometric data. Differential stress, σ', was obtained from subgrain size, D, using the following equation: σ' (MPa) = $107D^{-0.87}$ (μm). Strain rate, $\dot{e}'$, based on piezometric data, was calculated using Eq. (2).

Experimental run	Symbol		K0.8	Error	K1.1	Error	K1.5	Error	K1.85	Error	K2.2	Error	K2.5	Error
Deformation temperature	T	°C	345	0.1	345	0.1	345	0.1	345	0.1	345	0.1	345	0.1
Length of initial sample along X	dX	mm	43	0.5	43	0.5	43	0.5	43	0.5	43	0.5	43	0.5
Length of initial sample along Y	dY	mm	60	0.5	58	0.5	60	0.5	60	0.5	60	0.5	60	0.5
Length of initial sample along Z	dZ	mm	60	0.5	60	0.5	60	0.5	60	0.5	60	0.5	60	0.5
Initial thickness of anhydrite layer	Hi	mm	0.8	0.1	1.1	0.1	1.5	0.1	1.85	0.1	2.2	0.1	2.5	0.1
Finite strain along Y=Z	$e_Y = e_Z$		−0.32		−0.33		−0.33		−0.32		−0.33		−0.17	
Finite strain along X	e_X		1.16		1.22		1.22		1.16		1.22		0.44	
Finite longitudinal strain rate	$\dot{e}_{Y=Z}$	s^{-1}	−3.9E−07		−3.9E−07		−3.9E−07		−1.93E−07		−3.9E−07		−1.9E−07	
Maximum stress parallel to layer	$\sigma_{Y=Z//layer\ (max)}$	MPa	3.87		4.03		4.45		4.39		4.58		4.34	
Maximum stress perpendicular to layer	$\sigma_{Y=Z\ perp.\ layer\ (max)}$	MPa	1.49		3.86		4.52		2.39		3.85		2.11	
Maximum viscosity parallel to layer	$\eta_{Y=Z//layer\ (max)}$	Pa s	9.7E+12		1.0E+13		1.1E+13		2.2E+13		2.3E+13		2.2E+13	
Maximum viscosity perpendicular to layer	$\eta_{Y=Z\ perp.\ layer\ (max)}$	Pa s	3.7E+12		9.7E+12		1.1E+13		1.2E+13		1.9E+13		1.1E+13	
Post-fracture longitudinal strain	$e_{Y=Z\ (post\ fracture)}$		−0.05		−0.08		−0.07		−0.04		−0.08			
Number of analysed subgrains			71		292		120		138		201		278	
Mean subgrain size	D	mm	4.8E−02	1.3E−02	4.5E−02	1.4E−02	6.6E−02	1.9E−02	5.2E−02	1.8E−02	6.9E−02	2.2E−02	4.8E−02	2.1E−02
Maximum stress from subgrains	σ'_{max}	MPa	4.92		5.44		3.83		4.98		3.80		5.97	
Average stress from subgrains	σ'_{avr}	MPa	3.71		3.91		2.80		3.46		2.70		3.66	
Minimum stress from subgrains	σ'_{min}	MPa	3.00		3.08		2.23		2.68		2.11		2.68	
Maximum strain rate from piezometric data	$\dot{e}'_{max}$	s^{-1}	8.0E−07		1.1E−06		3.4E−07		8.3E−07		3.3E−07		1.5E−06	
Average strain rate from piezometric data	$\dot{e}'_{avr}$	s^{-1}	3.0E−07		3.6E−07		1.2E−07		2.4E−07		1.0E−07		2.9E−07	
Minimum strain rate from piezometric data	$\dot{e}'_{min}$	s^{-1}	1.5E−07		1.6E−07		5.4E−08		1.6E−07		4.5E−08		1.0E−07	

experimental runs. The microfabrics of the starting samples of anhydrite suggest that the latter did not undergo significant deformation under natural conditions. For this reason the microfabrics of the experimentally deformed samples should largely result from strain that was imposed by the experiments.

The open space in neck domains between anhydrite boudins, and the macroscopic outline of experimentally deformed anhydrite, suggest fracturing to be the principal deformation mechanism of anhydrite. Fracturing is also revealed by the microfabrics of anhydrite, particularly in neck domains. The fact that some of the microfractures are filled with organic matter suggests that fluid phases have played a role for fracturing and cataclasis (see below). Crystal plastic deformation, on the other hand, is portrayed by twins and undulatory extinction. Undulatory extinction results from translation gliding which is possible already at room temperature and at relatively low critical resolved shear stress, whereas twinning requires higher critical resolved shear stress and higher temperatures. In contrast to the starting samples of Gorleben anhydrite, the experimentally deformed samples display many more of twinned grains. Twinning is not efficient in accommodating large amounts of strain but is a powerful reorienting mechanism by creating volume in a twinned orientation (Müller et al., 1981). Twinning on {101} planes rotates the {001} planes in the twinned domain through 83.5° around an axis parallel to {010} pole, while the angle of shear is only 12.5° (Klassen-Neklyodova, 1964). It is interesting that twinning of anhydrite was probably not restricted to {101} planes, which are the common twin planes in anhydrite. The tightly spaced twin planes, oriented subperpendicular to the long axes of the anhydrite grains and thus perpencicular to the {101} planes, do not occur in the starting samples and thus must have developed during the experiments.

Although subgrains have not been observed in anhydrite, there is evidence for local recrystallization. The presence of serrated twin boundaries and serrated grain boundaries, the latter as contacts between large dirty old grains, on the one hand, and small but clear new grains, on the other hand, suggest that strain-induced grain-boundary migration was active as a thermally activated deformation process. The latter was driven by the movement of dislocations opposing work hardening by erasing grains of elevated stored strain energy. Recrystallization by grain-boundary migration has also been observed by Müller et al. (1981) in experimentally deformed anhydrite.

The microfabrics observed in the experimentally deformed anhydrite, thus, reflect the brittle–viscous transition and are fully consistent with those described for the brittle–viscous regime in the literature. Experiments carried out by Müller et al. (1981) and Ross et al. (1987) suggest the brittle–viscous regime to be characterized by twinning, kinking and microfracturing. The differential stresses applied during these experiments, however, were up to ca. 200 MPa and the effective viscosities were between 10^{14} and 10^{15} Pa s.

4.2. Deformation mechanisms in halite matrix

Evidence for dislocation creep of naturally deformed Asse halite is indicated by the presence of subgrains (Carter et al., 1982; Urai et al., 1987) and by weak crystallographic preferred orientation (Brokmeier, 1983). Moreover, fluid inclusions which are present on at least 80% of the grain boundaries, suggest that dissolution–reprecipitation creep has played a major role during natural deformation (Urai et al., 1987, see also Schenk and Urai, 2004). The Asse samples used for the present study, however, are largely free from a grain-shape fabric and do not show significant crystal plastic strain. As the strain imposed by the experiments is large (e_x = 120%), the weak initial fabrics can be neglected.

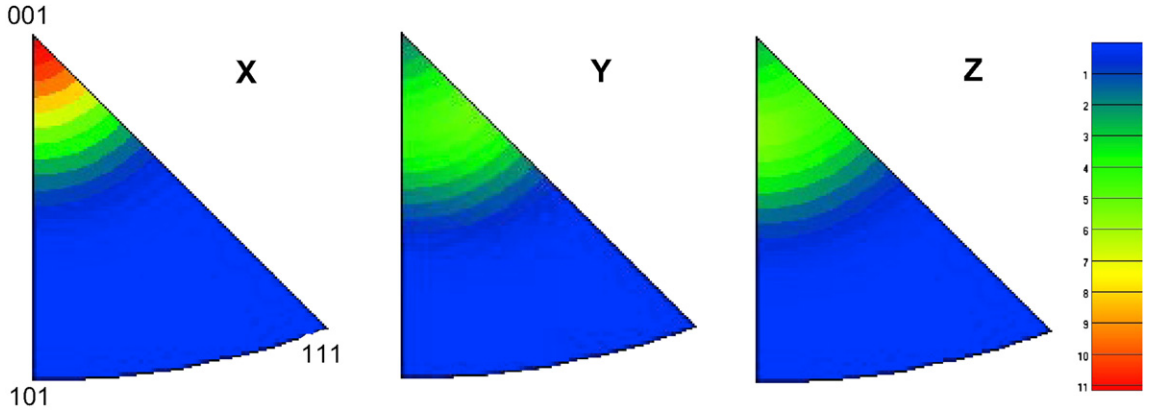

Fig. 7. Inverse pole figures of experimentally deformed halite matrix based on EBSD analyses. Equal-area upper-hemisphere projection. Half width = 15°; cluster size = 9°. Sample K1.85; analyzed section was cut parallel to the *X*-axis. Contour of 1 corresponds to a randomly orientated sample.

Viscous flow of halite during the constrictional experiments is indicated by the strong grain-shape fabric and by the fact that halite was able to flow into the necks between the rigid anhydrite boudins. The strongly folded old grain boundaries in sections cut perpendicular to the *X*-axis record the imposed constriction and have nothing to do with strain-induced grain-boundary migration. Serrated grain boundaries that might indicate grain-boundary migration are largely lacking.

EBSD analyses of experimentally deformed halite revealed a distinct 001-maximum (001-fibre texture) parallel to the *X*-axis. A similar texture was found by neutron diffraction analyses of Asse halite that was deformed under bulk constriction at $T = 300$ °C and $\dot{e}$ = ca. 1 s^{-1} (Skrotzki and Welch, 1983). These authors used a conventional extrusion press to deform halite under pure constriction, a circular billet being forced through a conical die. Because of the high-strain rate, however, stresses were much higher (ca. 700 MPa) compared to the stresses recorded in the present study.

The observed sets of tightly spaced bright lines, oriented at right angles in *X*-parallel irradiated sections (Fig. 6c), is an interesting microstructure that has not been described previously from deformed halite. As both the *X*-axis and the 100-direction bisect the bright lines, the latter should result from slip on {110}⟨110⟩ (planes hatched in blue in Fig. 10). Slip along this system also explains the chessboard like subgrain patterns in sections cut parallel to the *X*-axis. Since homogeneous crystal plastic strain requires the coeval activity of five independent slip systems, additional slip on {100}⟨110⟩ should have also been active during the experimental runs (Skrotzki and Haasen, 1981). As the fluids, and the organic matter in particular, lubricated the grain boundaries of the starting material, these inherited grain boundaries acted as planes with reduced shear strength. Slip along these boundaries is indicated by the distribution and stretch of fluid inclusions.

The differential stress obtained from the size of newly formed subgrains in halite is largely consistent with the actual stress recorded by the load cells of the machine, although not all of the prerequisites for piezometry are met. The stress-strain curves show a complex pattern and the cause of the strain hardening at advanced state of finite strain is still an open question. Weak to moderate strain hardening, however, does not have a significant impact on the piezometric data. It is difficult to explain why the stress range obtained from subgrains is more consistent with the red curves which reflect the higher stresses measured in the direction parallel to the anhydrite layer.

The presence of pervasive subgrains in the experimentally deformed samples suggests that dislocation creep processes have controlled the viscous deformation of Asse halite. In the present case of low stresses ($\sigma < 5$ MPa) steady-state flow can be approximated by the following equation (Carter et al., 1993):

$$\dot{e}' = 8.1 \times 10^{-5} \exp\left(-51.6/RT \cdot 10^{-3}\right) \sigma'^{3.4} \quad (2)$$

where strain rate, $\dot{e}'$, is expressed in s^{-1}, the pre-exponential constant is in MPa^{-n} s^{-1}, apparent activation energy is in J mol^{-1}, Boltzmann's gas constant, *R*, is in J mol^{-1} K^{-1}, temperature, *T*, is in K, differential stress, σ', is in MPa. The strain rates, $\dot{e}'$, obtained by inserting the piezometrically derived stresses, σ', into Eq. (2) are listed in Table 1 and are depicted in Fig. 11. All values show a large uncertainty with minimum and maximum values at 5.4×10^{-8} s^{-1} (sample K1.5) and 1.5×10^{-6} s^{-1} (sample K2.5), respectively. When comparing the calculated strain rates, $\dot{e}'$, with the actual strain rates, $\dot{e}$, it is obvious that in most cases the average value of $\dot{e}'$ is close to the strain rate adjusted during the individual runs (Fig. 11). Only in two of the samples (K1.5 and K2.2) the strain rate adjusted is outside the range of strain rates based on piezometrically derived stresses. Thus, Eq. (2) and the flow parameters obtained by Carter et al. (1993) for a temperature range of 50–200 °C can also be used to describe constrictional viscous flow of Asse halite at $T = 345$ °C and $\dot{e} = 10^{-7}$ s^{-1}. Moreover, the fact that subgrain formation played a major role during experimental deformation of Asse halite is consistent with observations by Carter et al. (1993) who revealed a major change in flow behavior with increasing stress and strain rate. This change in flow behavior is ascribed to a change in rate-limiting mechanisms from climb of edge disclocations, at low stress and strain rate (the present study), to cross-slip of screw dislocations at higher stress and strain rate. Subgrain formation in the present case of deformed Asse halite is also consistent with experimental results described by Franssen (1994) who found rotation of subgrains to be the main recrystallization mechanism at $T = 250$–450 °C implying strain hardening.

4.3. The role of fluids for deformation mechanisms of composite halite/anhydrite samples

A surprising feature of the experiments is the activity of fluid phases, although deformation occurred at $T = 345$ °C, and the total water content of Asse Na2SP samples is low (0.04 and 0.05 wt%, respectively, Urai et al., 1987; Gies et al., 1990). However, fluid inclusions are present not only in starting samples of Asse halite but also in those of Gorleben anhydrite, and in both cases they include organic matter as has been shown by fluorescence studies and Raman spectroscopy. The organic matter is forming the walls and

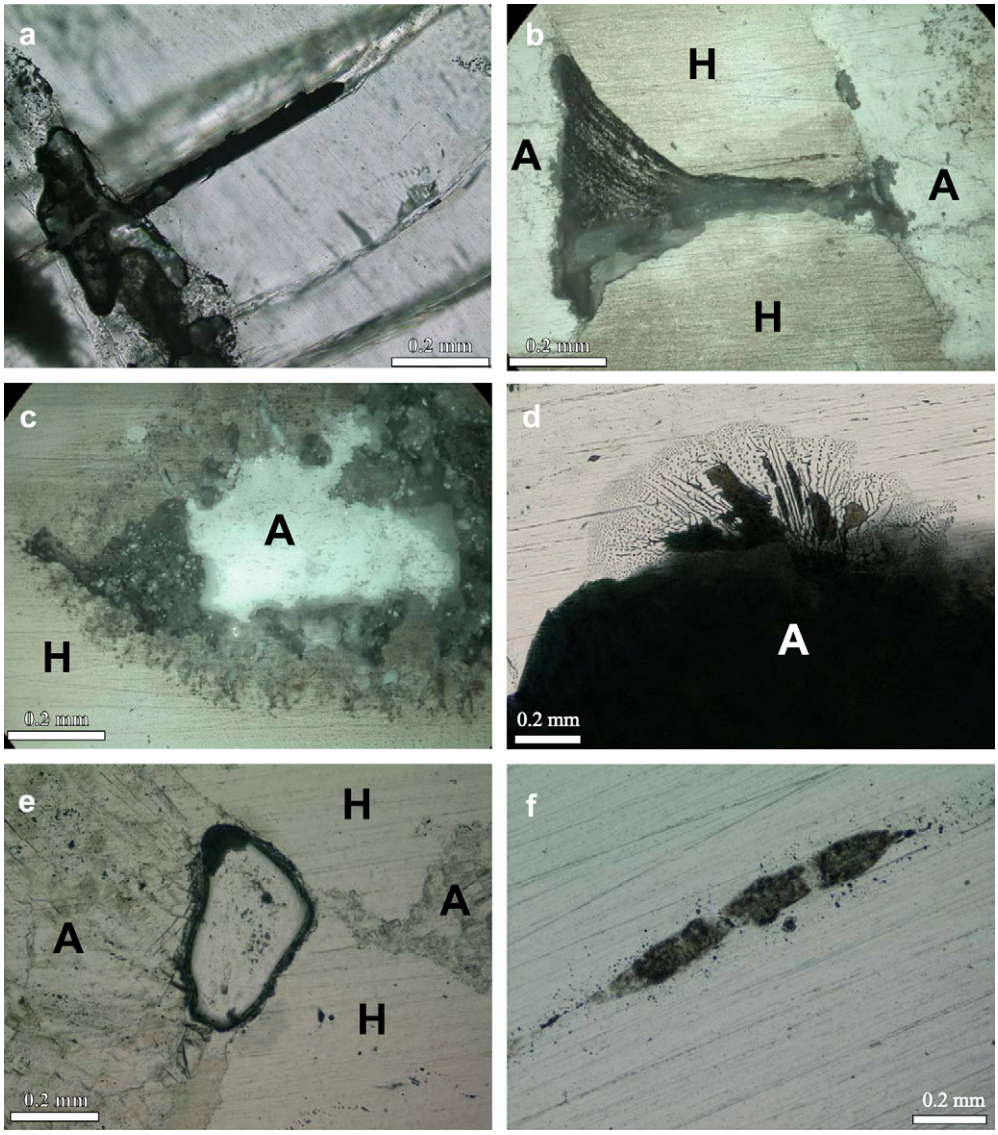

Fig. 8. Photomicrographs of neck domains, tension gashes and anhydrite–halite boundaries made with parallel polarizers. All sections cut parallel to the *X*-axis and perpendicular to anhydrite layer. A = anhydrite, H = halite. Note that pervasive thin dark lines in (c)–(f) result from sample polishing. (a) Tension fracture partly filled with dark organic matter is oriented subperpendicular the *X*-axis and grew during the final phase of constrictional deformation. Transmitted light. Sample K0.8. (b) Triangular shaped open space in neck domain coated with black organic matter. Reflected light. Sample K1.1. In-focus composite image based on stack of 9 photomicrographs. (c) Primary anhydrite inclusion in halite showing a corona consisting of radial fractures and fluid inclusions. Dark coating in pressure shadow (left side of anhydrite inclusion) consists of organic matter. Note the irregular boundary of the anhydrite. Reflected light. Sample K1.1. In-focus composite image based on stack of 8 photomicrographs. (d) Radial growth of rosette-shape fluid-inclusion trails into halite matrix nucleating at halite–anhydrite boundary. Thick section. Transmitted light. Sample K1.5. In-focus composite image based on stack of 15 photomicrographs. (e) Open cavity in neck domain with the walls coated with black organic matter and the rest being filled with fine-grained halite and minor organic matter which should have precipitated from fluid phase. Transmitted light. Sample K1.1. In-focus composite image based on stack of 5 photomicrographs. (f) Boudinage of primary anhydrite inclusion that was reoriented in viscous Asse halite. The long axis of the long-prismatic anhydrite is oriented subparallel to the *X*-axis. Note the fluid-inclusion halo surrounding the anhydrite boudins. Transmitted light. Sample K1.1.

the marginal part of the inclusions, whereas the central part consists of NaCl brine, at least in those of halite. The fluid inclusions in halite were strongly sheared, particularly at contacts to rigid anhydrite and thus could be expelled along microcracks or into the open spaces of neck domains. Migration of expelled fluids was particularly efficient in anhydrite because of the large number of microcracks which have formed during constriction. Thus, the microcracks in anhydrite enhanced the mobility of fluids, whereas the viscously flowing halite behaved as a sealing matrix. The intimate relation between the black coatings of open neck spaces and fluid inclusions is indicated by Raman spectra which indicate methane in both cases. Despite the high deformation temperature of 345 °C, the organic matter of deformed fluid inclusions and of black coatings of open neck spaces shows still fluorescence. This observation is surprising as fluorescence of organic matter is generally intense in shallow immature samples, decreases during diagenesis and most of catagenesis, but disappears entirely at the end of the oil zone (Ottenjann et al., 1974; Tissot and Welte, 1984).

There is evidence that at least parts of some fluids were expelled late during the experimental runs: (i) The tension gashes which developed subperpendicular to the *X*-axis are partly filled with organic matter. These gashes were opened in the final phase of the experimental runs after ca. 90% of strain was already imposed (Zulauf et al., 2009). (ii) The rosette-shaped fluid-inclusion trails, expelled from anhydrite boudins into the halite matrix, are largely undeformed and thus should have developed

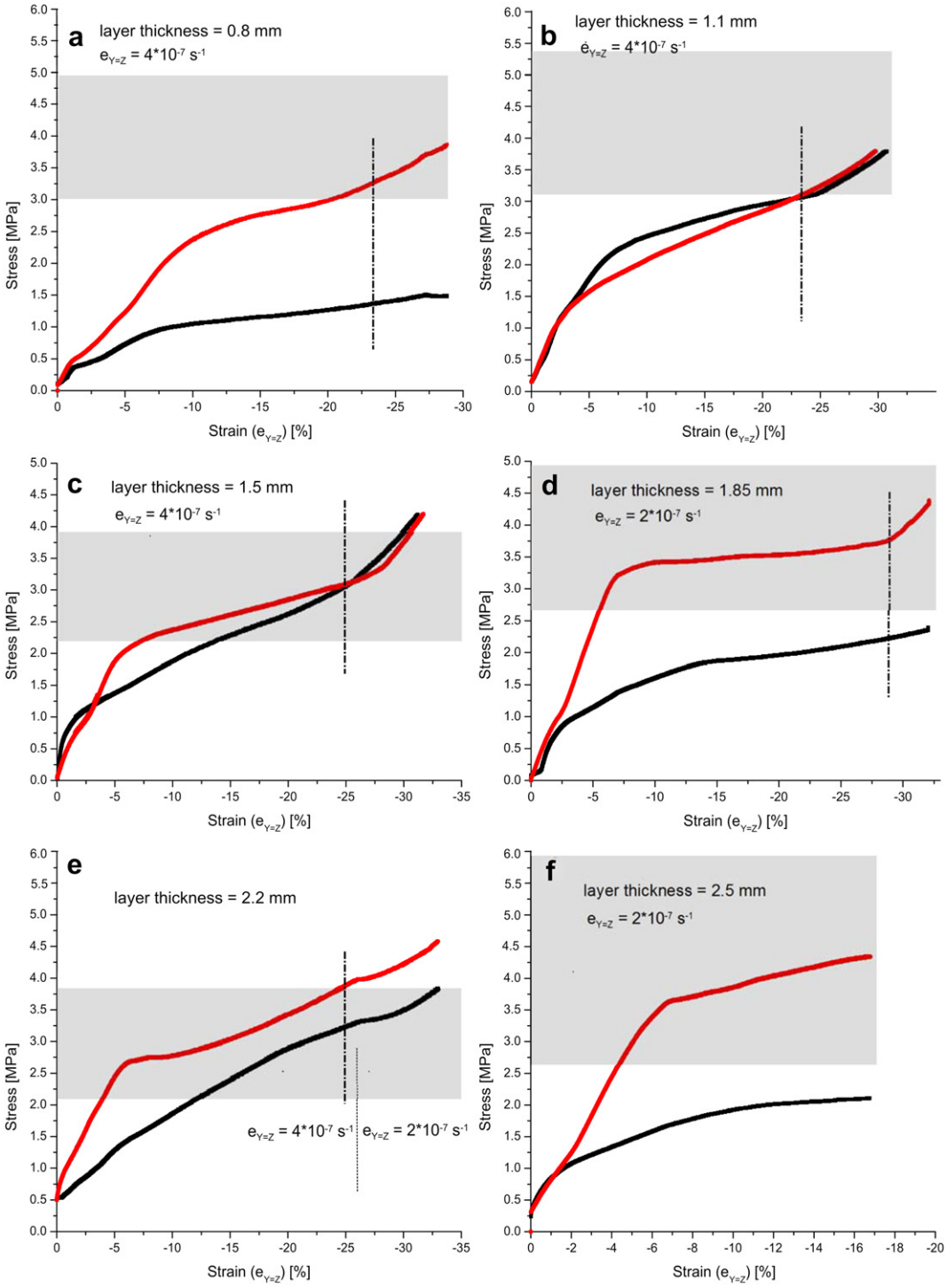

Fig. 9. Stress data obtained by piezometry based on subgrain size *D* of experimentally deformed Asse halite (shaded areas) as compared with actual stress-strain curves recorded by the load cells of the machine.

postkinematically. (iii) The black coating of neck domains seems to be undeformed.

There is evidence that some of the walls of the open space in neck domains was first coated with black organic matter and subsequently filled with fine-grained halite. As this type of fine-grained halite is entirely different compared to the viscously deformed halite of the matrix, it is interpreted to have formed by precipitation from a fluid phase. If this interpretation is true, the halite precipitated still later than the organic matter. Precipitation of white halite in the necks of anhydrite boudins has also reported from natural examples found in the Gorleben salt stock of northern Germany (Bornemann et al., 2008: Fig. 19).

The radial cracks in the halite matrix around primary anhydrite inclusions could indicate hydraulic fracturing due to elevated fluid pressure. Boudinage of the small anhydrite inclusions should also be supported by local elevated fluid pressure which led to reduction in principal stress. Finally it is possible that the pervasive tension gashes in the halite matrix, aligned subperpendicular to the *X*-axis,

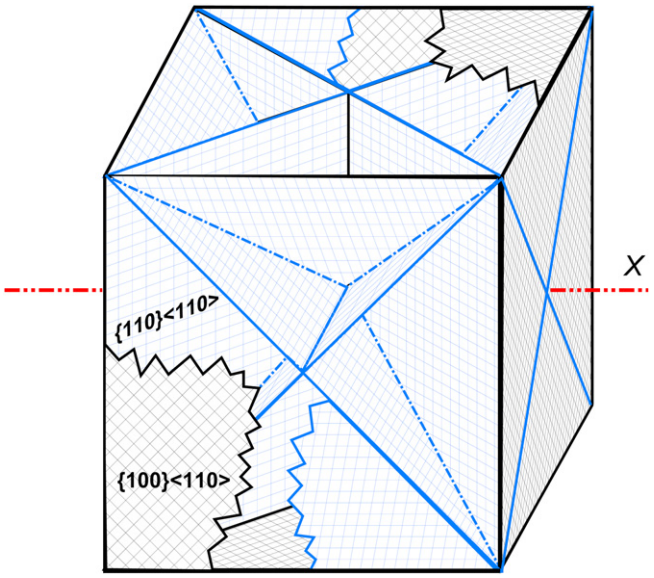

Fig. 10. Plot showing experimental strain rates compared with strain rates that were calculated using Eq. (2) and the stress values derived from subgrain size of halite. For further explanation, see text.

were opened because of elevated pore pressure. This assumption is supported by the fact that parts of the tension gashed are filled with black organic matter which should be derived from fluid inclusions.

Elevated fluid pressure during the experimental runs was not expected because the sample is unconfined and the system is open and fluids could escape. The fact that the fluid pressure could rise in the sample, although the system was open, suggests that the halite matrix was largely impermeable during viscous deformation.

Apart from the mechanical impact on the deforming sample, the fluids might also have an impact on viscous deformation. In a regime, where dislocation creep controls the rheology, the trace amount of brine plays an important role, as it drastically increases the grain-boundary mobility and induces dynamic recrystallization by fluid-assisted grain-boundary migration (e.g. Spiers and Carter, 1998; Watanabe and Peach, 2002). This impact, however, was probably low in the present study as evidence for grain-boundary migration is scarce in the deformed halite.

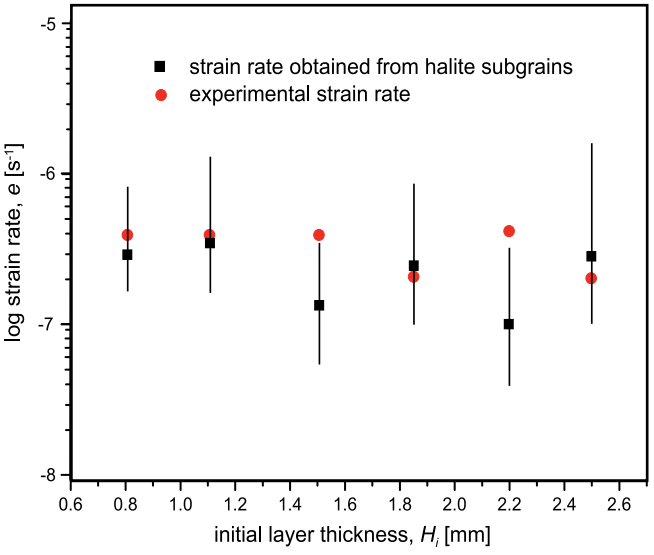

Fig. 11. Strain rate obtained from halite subgrains compared to actual strain rates used during the experiments.

4.4. Importance of the new results for salt tectonics and radioactive waste deposits

Active fluids are not restricted to the samples described in the present study. They are common constituents of late Permian (Zechstein) rock salt of northern Germany (e.g. Gropp, 1919; Ehrhardt, 1980; Fischer, 2000; Bornemann et al., 2008). The content of fluids in Asse halite is rather low (see above). In other salt stocks of northern Germany the water content varies between 0.1 and ca. 2% (Jockwer, 1981; Herrmann and Knipping, 1993). Gaseous and liquid hydrocarbons have been mapped during underground working using UV light. They are particularly frequent inside or close to rigid anhydrite layers and are often associated with late carnallite mineralization (Knistercarnallit, e.g. in Gorleben boreholes 1002, 1004, 1005, and 5001; Bornemann et al., 2008). Open fractures in anhydrite were forming reservoirs for fluids which led to replacement of anhydrite by polyhalite. Most of the liberated carbon hydrates include methane and are either primary constituents of the rock salt or are derived from organic matter that was a primary constituent of Staβfurt carbonate (z2SK) or of Rotliegend sediments (Bornemann et al., 2008, and references therein). Hydrocarbons in form of condensate represent a transitional phase between oil and gas in northern Germany. Gas phases inside fluid inclusions of the Gorleben salt consist of CH_4, H_2S, H_2, N_2, and O_2 (Siemann and Ellendorf, 2001). The most important phase inside the fluid inclusions is H_2O.

As all of the phenomena described above and in Part 1 of the present study (Zulauf et al., 2009) are common in salt domes of northern Germany, the new results should be important for workers who are dealing with radioactive waste deposits in rock salt. A survey on the long-term deposition of nuclear waste inside rock salt must consider possible pathways for fluids that might be enhanced by deformation causing release of radio nuclides and contamination of bed rock and biosphere. Release of liquid or gaseous hydrocarbons is also important for mine safety as large amounts of highly combustible hydrocarbons require particular safety measures during mining.

5. Conclusions

The following conclusions can be drawn from the present study:

- Deformation of halite–anhydrite sequences in salt domes is strikingly inhomogeneous because of the different deformation mechanism operating in both materials.
- Fluid inclusions inside both halite and anhydrite play a significant role during deformation.
- Brittle and brittle–ductile behavior of anhydrite is associated with dilatancy and formation of microfractures, the latter forming pathways for migrating fluids.
- Fluids which escaped from anhydrite did not penetrate deeply into halite, meaning the latter behaves as a sealing matrix. Given that anhydrite boudins are entirely enclosed in halite matrix, the fluids will stay inside the anhydrite. In cases where anhydrite forms continuous layers, which are free from boudinage or faulting, expelled fluids may migrate for long distances along microcracks of anhydrite and along halite–anhydrite boundaries.
- Future investigations should focus on the following open questions: (i) What is the 3D distribution of fluid inclusions of halite and anhydrite, (ii) is there a relation between grain-shape fabric and mechanical anisotropy in halite, (iii) what are the reasons for significant strain hardening during progressive deformation of halite.

Acknowledgements

We acknowledge constructive reviews by C. Talbot and H. Koyi both of which helped to improve the quality of the present paper. We are further grateful to M. Thomé and J.L. Urai for the help with the irradiated samples. Preparation of samples was performed by E. Gottwald and R. Götze. Fluorescence microscopy was supported by W. Schiller. All of their efforts are kindly acknowledged. Thanks also to BGR Hannover for providing samples of Asse halite and Gorleben anhydrite. This study was financially supported by Deutsche Forschungsgemeinschaft (DFG, grant Zu 73-13).

References

Bäuerle, G., 1998. Sedimentäre Texturen und Stylolithen am Top des Hauptanhydrits (Zechstein 3) im Salzstock Gorleben. Diploma thesis, Hannover University, Hannover, 97 pp. (unpublished).

Bestmann, M., Piazolo, S., Spiers, C.J., Prior, D.J., Franssen, R.C.M.W., 2005. Microstructural evolution during initial stages of static recovery and recrystallization: new insights from in-situ heating experiments combined with electron backscatter diffraction analysis. J. Struct. Geol. 27, 447–457.

Bornemann, O., Behlau, J., Fischbeck, R., Hammer, J., Jaritz, W., Keller, S., Mingerzahn, G., Schramm, M., 2008. Standortbeschreibung Gorleben, Teil 3: ergebnisse der über- und untertägigen Erkundung des Salinars. Geologisches Jahrbuch C73, 5–211. Hannover.

Brokmeier, H.G., 1983. Texturuntersuchungen an natürlichen und experimentell verfestigten Halitgesteinen mit Neutronen- und Wolfram Kα Strahlung. Ph.D. thesis, Technical University, Clausthal Zellerfeld, Germany, 160 pp.

Carter, N.L., Hansen, F.D., Senseny, P.E., 1982. Stress magnitudes in natural rock salt. J. Geophys. Res. 87, 9289–9300.

Carter, N.L., Horseman, S.T., Russell, J.E., Handin, J., 1993. Rheology of rocksalt. J. Struct. Geol. 15, 1257–1271.

Ehrhardt, K., 1980. Exploration eines neuen Baufeldes im Grubenbetrieb des Steinsalzwerkes Braunschweig-Lüneburg der Kali und Salz AG. In: Coogan, A.H., Hauber, L. (Eds.), Fifth Symposium on Salt, vol. 1. The Northern Ohio Geol. Soc, Cleveland, Ohio, USA, pp. 231–238.

Essaid, S., Klarr, K., 1982. Zum Innenbau der Salzstruktur Asse. Zeitschr. dt. geol. Ges. 133, 135–154. Hannover.

Fischer, M., 2000. Gefügekundliche Untersuchung von Steinsalz im Hinblick auf die Verteilung und Bindungsform von Kohlenwasserstoffen und die Bestimmung des Volumenanteils der Kohlenwasserstoff-Einschlüsse. Diploma thesis, University of Kiel, Germany, 60 pp. (unpublished).

Forster, B., Van De Ville, D., Berent, J., Sage, D., Unser, M., 2004. Complex wavelets for extended depth-of-field: a new method for the fusion of multichannel microscopy images. Microsc. Res. Tech. 65, 33–42.

Franssen, R.C.M.W., 1993. Rheology of synthetic rock salt with emphasis on the influence of deformation history and geometry on the flow behavior. PhD thesis, Rijksuniversiteit Utrecht.

Franssen, R.C.M.W., 1994. The rheology of synthetic rocksalt in uniaxial compression. Tectonophysics 233, 1–40.

Gies, H., Herbert, H.-J., Jockwer, N., 1990. Zur Bedeutung der Wassergehalte für die Lithostratigraphie in Steinsalzhorizonten des Zechsteins. Kali und Steinsalz 10, 265–271.

Gropp, H., 1919. Gasvorkommen in Kalisalzbergwerken in den Jahren 1907 bis 1917. Kali 3, 33–42 (Halle).

Guillopé, M., Poirier, J.P., 1979. Dynamic recrystallization during creep of single-crystalline halite: an experimental study. J. Geophys. Res. 84, 5557–5567.

Herrmann, A.G., Knipping, B., 1993. Fluide Komponenten als Teile des Stoffbestandes der Evaporite im Salzstock Gorleben. Vorkommen, Herkunft, Entstehung und Wechselwirkungen mit den Salzgesteinen. Technical University of Clausthal, Institit für Mineralogie und Mineralogische Rohstoffe, Clausthal-Zellerfeld, 140 pp.

Hickman, S.H., Evans, B., 1991. Experimental pressure solution in halite: the effect of grain/interphase boundary structure. J. Geol. Soc. Lond. 148, 549–560.

Hiraga, H., Shimamoto, T., 1987. Textures of sheared halite and their implications for the seismogenetic slip of deep faults. Tectonophysics 144, 69–86.

Jockwer, N., 1981. Untersuchungen zu Art und Menge des im Steinsalz des Zechsteins enthaltenen Wassers sowie dessen Freisetzung und Migration im Temperaturfeld endgelagerter radioaktiver Abfälle. GSF, Institut für Tieflagerung, Wiss. Abt., GSF-Bericht, T119, 134 pp, Braunschweig.

Klassen-Neklyodova, M.V., 1964. Mechanical Twinning of Crystals. Consultants Bureau, New York, N.Y., 87 pp.

Li, Y.P., Yang, C.H., Qian, Q.H., Wei, D.H., Qu, D.A., 2007. Experimental research on deformation and failure characteristics of laminated Salt Rock. In: Wallner, M., Lux, K.-H., Minkley, W., Hardy, Jr., H.R. (Eds.), The Mechanical Behavior of Salt – Understanding of THMC Processes in Salt. Taylor & Francis Group, London, pp. 69–74.

Müller, W.H., Schmid, S.M., Briegel, U., 1981. Deformation experiments on anhydrite rocks of different grain sizes: rheology and microfabric. Tectonophysics 78, 527–543.

Ottenjann, K., Teichmüller, M., Wolf, M., 1974. Spektrale Fluoreszenz-Messungen an Sporiniten mit Auflicht-Anregung, eine mikroskopische Methode zur Bestimmung des Inkohlungsgrades gering inkohlter Kohlen. Fortschr. Geol. Rheinl. Westf. 24, 1–36.

Pennock, G.M., Drury, M.R., Spiers, C.J., 2005. The development of subgrain misorientations with strain in dry synthetic NaCl measured using EBSD. J. Struct. Geol. 27, 2159–2170.

Popp, T., Wiedemann, M., Kansy, A., Pusch, G., 2007. Gas transport in dry rock salt – implications from laboratory investigations and field studies. In: Wallner, M., Lux, K.-H., Minkley, W., Hardy Jr., H.R. (Eds.), The Mechanical Behavior of Salt – Understanding of THMC Processes in Salt. Taylor & Francis Group, London, pp. 17–26.

Ross, J.V., Bauer, S.J., Hansen, F.D., 1987. Textural evolution of synthetic anhydrite–halite mylonites. Tectonophysics 140, 307–326.

Schenk, O., Urai, J.L., 2004. Microstructual evolution and grain boundary structure during static recrystallization in synthetic polycrystals of sodium chloride containing saturated brine. Contrib. Mineral. Petrol. 146, 671–682.

Schléder, Z., Urai, J.L., 2005. Microstructural evolution of deformation-modified primary halite from the middle triassic Röt Formation at Hengelo, The Netherlands. Int. J. Earth Sci. 94, 941–955.

Schléder, Z., Urai, J.L., 2007. Deformation and recrystallization mechanisms in mylonitic shear zones in naturally deformed extrusive Eocenee Oligocene rocksalt from Eyvanekey plateau and Garmsar hills (central Iran). J. Struct. Geol. 29, 241–255.

Siemann, M.G., Ellendorf, B., 2001. The composition of gases in fluid inclusions of late Permian (Zechstein) marine evaporites of Northern Germany. Chem. Geol. 173, 31–44.

Skrotzki, W., Haasen, P., 1981. Hardening mechanisms of ionic crystals on {110} and {100} slip planes. J. Phys. 42 (C3), 119–148.

Skrotzki, W., Welch, P., 1983. Development of texture and microstructure in extruded ionic polycrystalline aggregates. Tectonophysics 99, 47–61.

Spiers, C.J., Schutjens, P.M.T.M., 1990. Densification of crystalline aggregates by fluid-phase diffusional creep. In: Barber, D.J., Meredith, P.G. (Eds.), Deformation Processes in Mineral Ceramics and Rocks. Unwin Hyman, Boston, pp. 334–353.

Spiers, C.J., Carter, N.L., 1998. Microphysics of rocksalt flow in nature. In: Aubertin, M., Hardy, H.R. (Eds.), The Mechanical Behaviour of Salt: Proceedings of the Fourth Conference Series on Rock and Soil Mechanics, vol. 22. TTP Trans Tech Publications, Clausthal-Zellerfeld, pp. 115–128.

Spiers, C.J., Schutjens, P.M.T.M., Brzesowsky, R.H., Peach, C.J., Liezenberg, J.L., Zwart, H.J., 1990. Experimental determination of constitutive parameters governing creep of rocksalt by pressure solution. In: Knipe, R.J., Rutter, E.H. (Eds.), Deformation Mechanisms, Rheology, and Tectonics. Geol. Soc. London, Special Publ., vol. 54, pp. 215–227.

Ter Heege, J.H., De Bresser, J.H.P., Spiers, C.J., 2005b. Rheological behavior of synthetic rocksalt: the interplay between water, dynamic recrystallization and deformation mechanisms. J. Struct. Geol. 27, 948–963.

Tissot, B.P., Welte, D.H., 1984. Petroleum Formation and Occurrence. Springer, Berlin, Heidelberg, New York, Tokyo, 699 pp.

Twiss, R.J., Moores, E.M., 1992. Structural Geology, 532 pp. W.H. Freeman & Co, New York.

Twiss, R.J., 1977. Theory and applicability of a recrystallized grain size paleopiezometer. Pure Appl. Geophys. 115, 225–244.

Urai, J.L., Spiers, C.J., 2007. The effect of grain boundary water on deformation mechanisms and the rheology of rocksalt during long-term deformation. In: Wallner, M., Lux, K.-H., Minkley, W., Hardy Jr., H.R. (Eds.), The Mechanical Behavior of Salt – Understanding of THMC Processes in Salt. Taylor & Francis Group, London, pp. 149–158.

Urai, J.L., Spiers, C.J., Peach, C.J., Franssen, R.C.M.W., Liezenberg, J.L., 1987. Deformation mechanisms operating in naturally deformed halite rocks as deduced from microstructural investigations. Geol. Mijnbouw 66, 165–176.

Watanabe, T., Peach, C., 2002. Electrical impedance measurement of plastically deforming halite rocks at 125°C and 50 MPa. J. Geophys. Res. 107 (B1), 2–12. ECV 2-1-ECV.

Zulauf, G., Zulauf, J., Bornemann, O., Kihm, N., Peinl, M., Zanella, F., 2009. Experimental deformation of a single-layer anhydrite in halite matrix under bulk constriction. Part 1: geometric and kinematic aspects. J. Struct. Geol., doi:10.1016/j.jsg.2009.01.013 published online.